Chemical Science

ROYAL SOCIETY OF CHEMISTRY

EDGE ARTICLE

View Article Online
View Journal | View Issue

Cite this: *Chem. Sci.*, 2025, **16**, 7366

All publication charges for this article have been paid for by the Royal Society of Chemistry

Thiophene-backbone arcuate graphene nanoribbons: shotgun synthesis and length dependent properties†

Ruiying Zhang,[a] Xinyu Chen,[a] Lingyun Zhu,[a] Yanxia Huang,[a] Zi'ang Zhai,[a] Qiang Wang,[a] Lingding Wang,[a] Taosong Wang,[a] Wei-Zhen Wang,[a] Ke-Yin Ye *[a] and Yuanming Li *[ab]

Received 10th December 2024
Accepted 18th March 2025

DOI: 10.1039/d4sc08353a

rsc.li/chemical-science

Efficient synthetic methods are urgently needed to produce graphene nanoribbons (GNRs) with diverse structures and functions. Precise control over the topological edges of GNRs is also crucial for achieving diverse molecular topologies and desirable electro-optical properties. This study demonstrates a highly efficient "shotgun" synthesis of thiophene-backbone arcuate GNRs, offering a significant advantage over tedious iterative synthesis. This method utilizes a one-pot, three component Suzuki–Miyaura coupling for the precursor, followed by a Scholl reaction for cyclization. The resulting arcuate GNRs have sulfur atoms embedded in the carbon backbone with a combined armchair, cove, and fjord edge structure. This multi-edge architecture is further modified by high-yield oxidation of the electron-rich sulfur atoms to electron-deficient sulfones, enabling precise regulation of the GNRs' electronic properties. These arcuate GNRs with diverse edge structures, heteroatom doping and precise lengths open exciting avenues for their application in optoelectronic devices.

Introduction

Atomically precise graphene nanoribbons (GNRs) have attracted significant attention recently due to their intriguing electronic properties and applications in next-generation optoelectronic devices.[1–8] Their optical and electronic properties strongly depend on their structural parameters, such as lengths, widths, shapes, and edges.[9–13] Besides control over the above-mentioned structural parameters, properties can be fine-tuned by incorporation of heteroatoms into the conjugated nanoribbon backbones.[14–17] Organic chemists have focused on developing new synthetic strategies and easily accessible structure-rich building blocks for the production of GNRs and heteroatom-doped GNRs over decades.[18–21]

The solution-phase synthesis that is the formation of a linearly extended precursor followed by a ring-closing step is one of the most promising strategies for the preparation of well-defined GNRs on a large scale.[22–30] For the study of length-dependent photophysical properties *via* comparison with their linear counterparts, GNRs with different lengths are usually prepared by iterative synthesis (Fig. 1a).[12,17,31,32] These methods often involve complex and expensive starting materials,

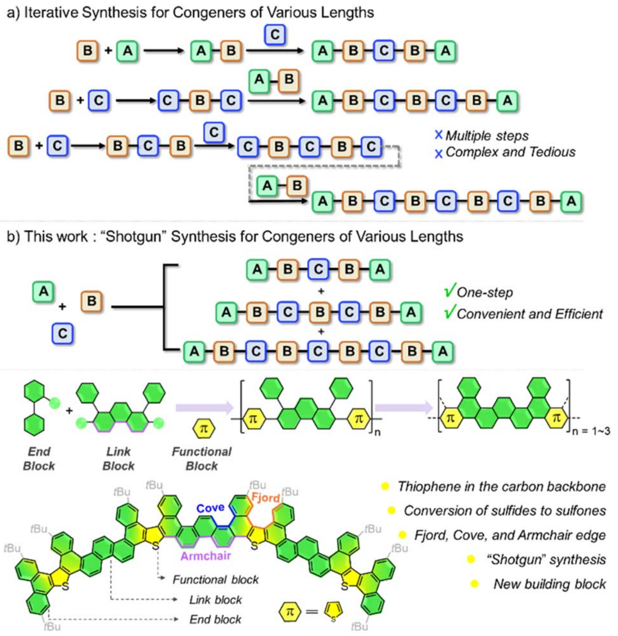

Fig. 1 Synthesis of thiophene-backbone arcuate graphene nanoribbons. (a) The precursor of GNRs was constructed by an iterative strategy. (b) Schematic illustration of rapid construction of thiophene-backbone arcuate GNRs.

---

[a] *Key Laboratory of Molecule Synthesis and Function Discovery, Fujian Province University, College of Chemistry at Fuzhou University, Fuzhou, Fujian, 350108, China. E-mail: yuanming.li@fzu.edu.cn; kyye@fzu.edu.cn*

[b] *State Key Laboratory of Elemento-Organic Chemistry, Nankai University, Tianjin, 300071, China*

† Electronic supplementary information (ESI) available. CCDC 2303698 and 2303699. For ESI and crystallographic data in CIF or other electronic format see DOI: **https://doi.org/10.1039/d4sc08353a**

restricting structural and functional diversity. The "shotgun" approach to macrocycles[33–37] involves using a one-pot multicomponent cyclization of small monomers, to access the macrocycle. This approach shows great advantages to quickly construct macrocycles with diverse sizes and functionalities. In addition, phenanthrene is an important polycyclic aromatic hydrocarbon (PAH), which has an armchair side. We envision that 1,8-diaryl phenanthrene derivatives would be promising building blocks for the "shotgun" synthesis of GNRs, which are readily available.[38]

Herein, we report a series of arcuate GNRs with thiophene backbones with high efficiency. The precursor of GNRs was constructed by Suzuki–Miyaura coupling with 1,8-diaryl phenanthrene as a key building block and then dehydrogenation to obtain GNRs of different lengths. In this case, three GNRs (**AR-11**, **AR-17**, and **AR-23**) with multiple edge structures were achieved (the numbering indicates the number of longitudinally fused rings along their backbone) (Fig. 1a). Oxidizing electron-rich sulfur atoms to electron-deficient sulfones yielded **ARO-11** and **ARO-17** with high efficiency, respectively. Detailed theoretical and experimental studies demonstrate that length and the oxidation state greatly affect not only molecular conformations but also electronic structures and photophysical properties.

Results and discussion

Synthesis

To achieve the synthesis of GNRs, a key building block, that is, 1,8-diaryl phenanthrene-2,7-diboronic acid pinacol ester **3** was synthesized in three steps on a gram scale (Scheme S2†),[38] which features armchair and cove type edges (Scheme 1a). The introduction of sulfur into GNRs is achieved by the addition of 2,5-dibromothiophene **2** as the functional block. In addition, 2-substituted biphenyl **1** was introduced as the end block. *Tert*-butyl substituents were installed respectively on **1** and **3** to ensure the good solubility of the intermediates and the corresponding GNRs. With the key link block **3**, functional block **2**, and end block **1** in hand, a series of precursors of sulfur-doped **AR-*n*** were obtained by one-pot synthesis and isolated through column chromatography in 53% (**4a**), 19% (**4b**), and 12% (**4c**) yield, respectively. By varying the end groups and adjusting the molar ratio of the three components, congeners with diverse lengths can be obtained (see Scheme S3 and Table S2† for further details).[39] This "shotgun" approach demonstrates

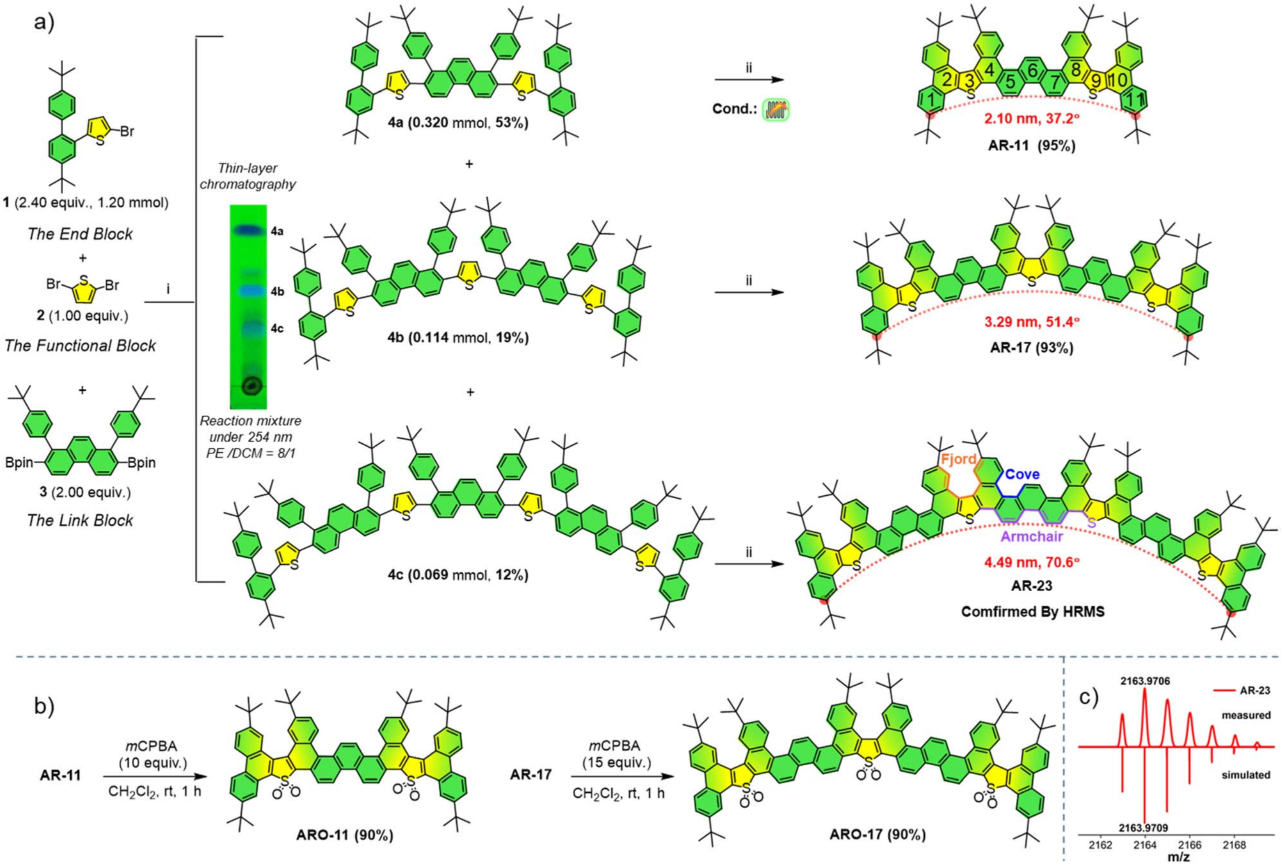

Scheme 1 The synthesis of thiophene-backbone arcuate GNRs. (a) (i) **1** (2.4 equiv.), **2** (1.0 equiv.), **3** (2.0 equiv.), $Pd(PPh_3)_4$ (0.5 equiv.), K_2CO_3 (25 equiv.), 1,4-dioxane: $H_2O = 8:1$; 90 °C, 36 h. Isolated yields were based on the amount of compound **1**. Thin-layer chromatography: TLC was run three times with the eluent system (PE/DCM = 8/1). (ii) DDQ (1.2 equiv. for each C–C bond), CF_3SO_3H, CH_2Cl_2, −10 °C, 1 h. DDQ: 2,3-dichloro-5,6-dicyano-1,4-benzoquinone. Electrochemical continuous flow conditions: a carbon anode, a Ni cathode, $^{n}Bu_4NBF_4$(0.13 M), DCM/TFA, **4a** (0.1 mmol), 1.65 V, 0.10 mL min^{-1}, rt. (b) Synthetic route of **ARO-11** and **ARO-17**. (c) High-resolution MALDI-TOF mass spectra of **AR-23**.

significant advantages over conventional iterative synthesis in terms of time efficiency and material economy. A direct comparison reveals that the iterative strategy requires six reactions spanning 216 hours to produce **4a**, **4b**, and **4c**, while our protocol achieves identical product formation in just 36 hours (an 84% reduction in total reaction time). Critically, this method also exhibits marked improvement in synthetic economy: equimolar quantities of target products can be obtained using significantly less starting material compared to the traditional approach (Scheme S4†). The drastic reduction in both operational steps (from six to one) and experimental duration highlights the exceptional practicality and scalability of this synthesis strategy for multi-component molecular construction.

The following ring-closing reactions of **4a** and **4b** by intramolecular oxidative cyclodehydrogenation in the presence of 2,3-dichloro-5,6-dicyano-1,4-benzoquinone (DDQ) and CF_3SO_3H gave the desired GNRs **AR-11** and **AR-17** in 95% and 93% yields, which were well-characterized by NMR analysis and HRMS. Due to the poor solubility of **AR-23**, well-resolved ^1H and ^{13}C NMR spectra could not be recorded. However, characterization was achieved by matrix-assisted laser desorption/ionization time-of-flight mass spectrometry (MALDI-TOF MS), Fourier transform infrared spectroscopy (FT-IR) and the Raman spectrum (Scheme 1c and Fig. S6–S8†). The Scholl reaction is conducted using super stoichiometric oxidants, limiting its scalability. To address these challenges, we also developed an electrochemical continuous flow Scholl reaction. This method eliminates the need for oxidants and enables the production of **AR-11** in larger quantities. The arc lengths and radians of **AR-11**, **AR-17** and **AR-23** are 2.10 nm and 37.2° for **AR-11**, 3.29 nm and 51.4° for **AR-17**, and 4.49 nm and 70.6° for **AR-23** based on density functional theory (DFT) optimized structures (Scheme 1a and Fig. S9–S13†). The source code of the program for the measurement of lengths and the radians is listed in Table S5.† In addition, **AR-11** and **AR-17** were oxidized to give orange solid **ARO-11** and **ARO-17** with excessive *meta*-chloroperoxybenzoic acid (*m*CPBA) in 90% yields (Scheme 1b).

X-ray crystal structures

The arcuate and curved shape structures of **AR-11** and **ARO-11** were confirmed by single-crystal X-ray diffraction analysis (Fig. 2). Slow diffusion of acetone into a $CDCl_3/CS_2$ solution of **AR-11** at room temperature resulted in the formation of **AR-11** single crystals. The single crystals of **ARO-11** were obtained by the slow diffusion of CH_3OH into the $CHCl_3$ solution. Single-crystal structure analysis indicated that the π-skeletons of **AR-11** and **ARO-11** are highly twisted along their longitudinal axes (Fig. 2a and b). With the presence of bulky *tert*-butyl groups on the fjord edges of **AR-11** and **ARO-11**, the benzenoid rings adopt an interlacing "up–down" conformation with dihedral angles ranging from 36° to 47° (also see Fig. S2†). The end-to-end arc lengths for the π-backbone of **AR-11** and **ARO-11** are 2.05 nm and 2.06 nm, respectively, which correspond to the DFT optimized structures (Scheme 1a). In the packing structures of **AR-11** and **ARO-11** (Fig. 2c and d), every two identical molecules

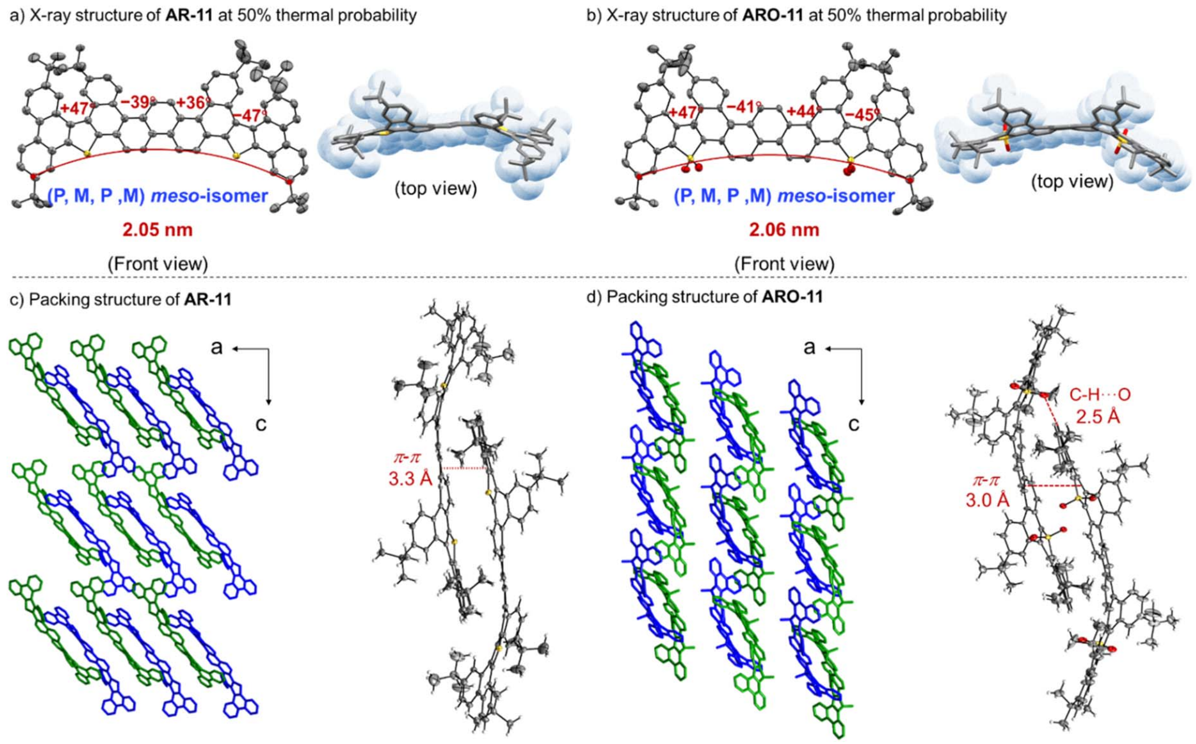

Fig. 2 Crystal structures of AR-11 and ARO-11. (a and b) X-ray crystal structures of AR-11 and ARO-11. (Thermal ellipsoids are shown at 50% probability). (c and d) The packing structure of AR-11 and ARO-11. (Solvent molecules, hydrogen atoms and partial tertiary butyl are omitted for clarity).

(shown in green and blue) surround each other in the form of face to edge, forming a dimer. This dimer presents a slip-stacked packing mode along the plane of the *a*-axis and *c*-axis. In the stacking structures of **AR-11**, the dimer has intermolecular π–π interactions with an interlayer distance as short as 3.3 Å (Fig. 2c and S2b†). In the crystal structure of **ARO-11** the distance of π–π interactions between the adjacent molecules is 3.0 Å. Besides, there are face-to-edge intermolecular C–H…O hydrogen bonding interactions (2.5 Å) and the arrangement is closer for **ARO-11** (Fig. 2d and S2b†).

Calculations and photophysical properties

Considering the 4-fold helicity of **AR-11**, we can depict ten stereoisomers including four pairs of enantiomers and two meso isomers (six diastereomers in total, Fig. 3), which are categorized as follows: C_1 symmetry (C_1-I and C_1-II), C_2 symmetry (C_2-I and C_2-II), and C_s symmetry (C_s-I and C_s-II) (Fig. 3). Density Functional Theory (DFT) calculations were performed to explore their relative stability. Calculation details are given in the ESI (Fig. S14 and S15)†[40–46] Based on the DFT calculations, the (*P*,*M*,*P*,*M*) conformation is the most stable, which is consistent with the X-ray crystal structure result, followed by the alternated (*P*,*M*,*M*,*P*) (+0.9 kcal mol^{-1}). The conversion barrier of **AR-11** from the (*P*,*M*,*M*,*P*) to the (*P*,*M*,*P*,*M*) is 20.1 kcal mol^{-1} (Fig. S15†). Furthermore, **AR-17** exhibits 6-fold helicity and affords 36 types of isomers with varying Gibbs free energies (Fig. S16†). Semi-empirical calculations were conducted over them. Based on the calculations, the (*P*,*M*,*P*,*M*,*P*,*M*,*P*) conformation is the most stable, followed by the alternated conformation (*P*,*M*,*P*,*M*,*P*,*P*,*M*) (+0.8 kcal mol^{-1}).

To gain insight into the length-dependent photophysical properties of **AR-*n*** and **ARO-*n***, UV/vis absorption and fluorescence emission were measured in diluted CH_2Cl_2 solutions at room temperature (Fig. 4a and b). The results are summarized in Table 1. **AR-17** (λ_{abs} = 434 nm, log ε = 5.24) exhibited a bathochromic shift compared to **AR-11** (λ_{abs} = 415 nm, log ε = 5.07), which was attributed to the extended π-backbone. **ARO-11** exhibited a pronounced bathochromic shift in its absorption maximum (λ_{abs} = 466 nm, log ε = 4.79) compared to **AR-11** as well, attributable to the integration of the electron-withdrawing thiophene-*S*,*S*-dioxide unit into the extended π-system. Notably, **ARO-11** displayed broader absorption features than **AR-11**. Similar trends were observed for **ARO-17** and **AR-17**.

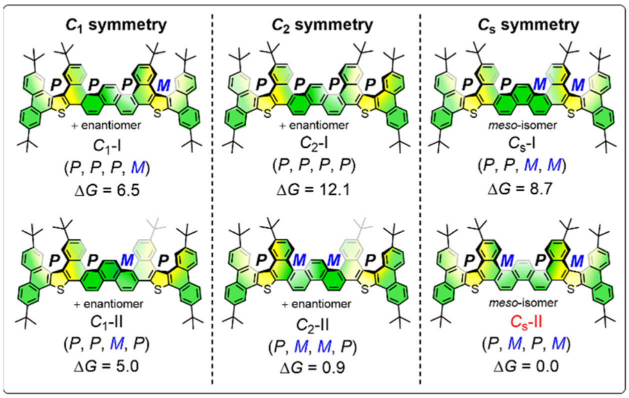

Fig. 3 Stereoisomers of AR-11 and their relative Gibbs free energies (kcal mol^{-1}).

Compared to **AR-11** (λ_{em} = 459 nm), the bathochromic shift in the photoluminescence spectra was pronounced for **AR-17** (λ_{em} = 479 nm) due to its extended conjugated backbone, or for **ARO-11** (λ_{em} = 511 nm) due to incorporation of the electron-withdrawing thiophene-*S*,*S*-dioxide unit (Fig. 4b). The absolute fluorescence quantum yields (Φ_F) were measured by using an integrating sphere detector.[47] In CH_2Cl_2 solution, Φ_F values increased with π-backbone extension in **AR-11** (15%) and **AR-17** (37%). Conversely, **ARO-11** (65%) and **ARO-17** (71%) displayed high, π-backbone-independent Φ_F values. In the solid state, however, Φ_F values decreased to 5.9% for **ARO-11** and 1.5% for **ARO-17**, likely due to aggregation-caused quenching *via* strong intermolecular π-overlap. Similar trends were observed for **AR-11** (4.7%) and **AR-17** (0.2%).[48–50] Additionally, the emission wavelengths of the compounds in the solid state were measured. Owing to the high molecular rigidity of the compounds, the emission wavelengths in both the solid and solution states showed minimal red-shift (Fig. S5†). To further elucidate the photophysical properties, the energy diagrams and frontier molecular orbitals of **AR-*n*** and **ARO-*n*** were calculated by the time-dependent density functional theory (TD-DFT) method at the PBE0-D3(BJ)/6-31G(d,p) level of theory (Fig. 4d, S19 and S20†).[51] The lowest energy absorption bands of **AR-*n*** and **ARO-*n*** are attributed to the $S_0 \rightarrow S_1$ excitation (Δ*E*, 3.12 eV for **AR-11**, 2.74 eV for **ARO-11**, 2.97 eV for **AR-17**, and 2.61 eV for **ARO-17**), which mainly arises from the HOMO → LUMO transition (95% for **AR-11**, 92% for **ARO-11**, 90% for **AR-17**, and 87% for **ARO-17**) and has an oscillator strength (*f*) of 1.77 for **AR-11**, 1.19 for **ARO-11**, 3.07 for **AR-17**, and 2.11 for **ARO-17** (Tables S6–S9†). The electrochemical properties of these sulfur-doped GNRs were studied in CH_2Cl_2 solution by cyclic voltammetry (CV) and differential pulse voltammetry (DPV). All compounds exhibited an obvious reduction process, with Ep^{red1} values of −1.51 eV (**AR-11**), −1.76 eV (**ARO-11**), −1.52 eV (**AR-17**), and −1.57 eV (**ARO-17**). Oxidation potentials (Ep^{ox1}) were 0.65 eV (**AR-11**), 0.74 eV (**ARO-11**), 0.80 eV (**AR-17**), and 0.92 eV (**ARO-17**). Based on Ep^{ox1} values, HOMO energy levels were estimated to be −5.34 eV (**AR-11**), −5.60 eV (**ARO-11**), −5.66 eV (**AR-17**), and −5.41 eV (**ARO-17**), demonstrating good agreement with the computational study (Fig. 4c, S3† and Table 1).

The energy levels of the calculated frontier molecular orbitals of **AR-*n*** and **ARO-*n*** are shown in Fig. 4d, S19 and S20,† for example, the HOMO and LUMO of **AR-17** and **ARO-17** spread over the whole π-system. After converting the electron-rich thiophene ring into an electron-poor thiophene-*S*,*S*-dioxides, the sulfone dioxide unit considerably reduces the HOMO energy level; the LUMO energy level has a greater decrease. Hence, the energy gap of the molecule is greatly reduced, which leads to a large redshift of fluorescence emission. Notably, the band gaps of **AR-*n*** and **ARO-*n*** are well regulated from 3.90 eV of **AR-5** to 3.11 eV of **AR-23** and 3.43 eV of **ARO-5** to 2.81 eV of **ARO-23**. The energies of frontier orbitals of **AR-*n*** and **ARO-*n*** are plotted in Fig. 4e (also see Fig. S21–S24†). The decrement of the LUMO energy level and increment of the HOMO energy level are

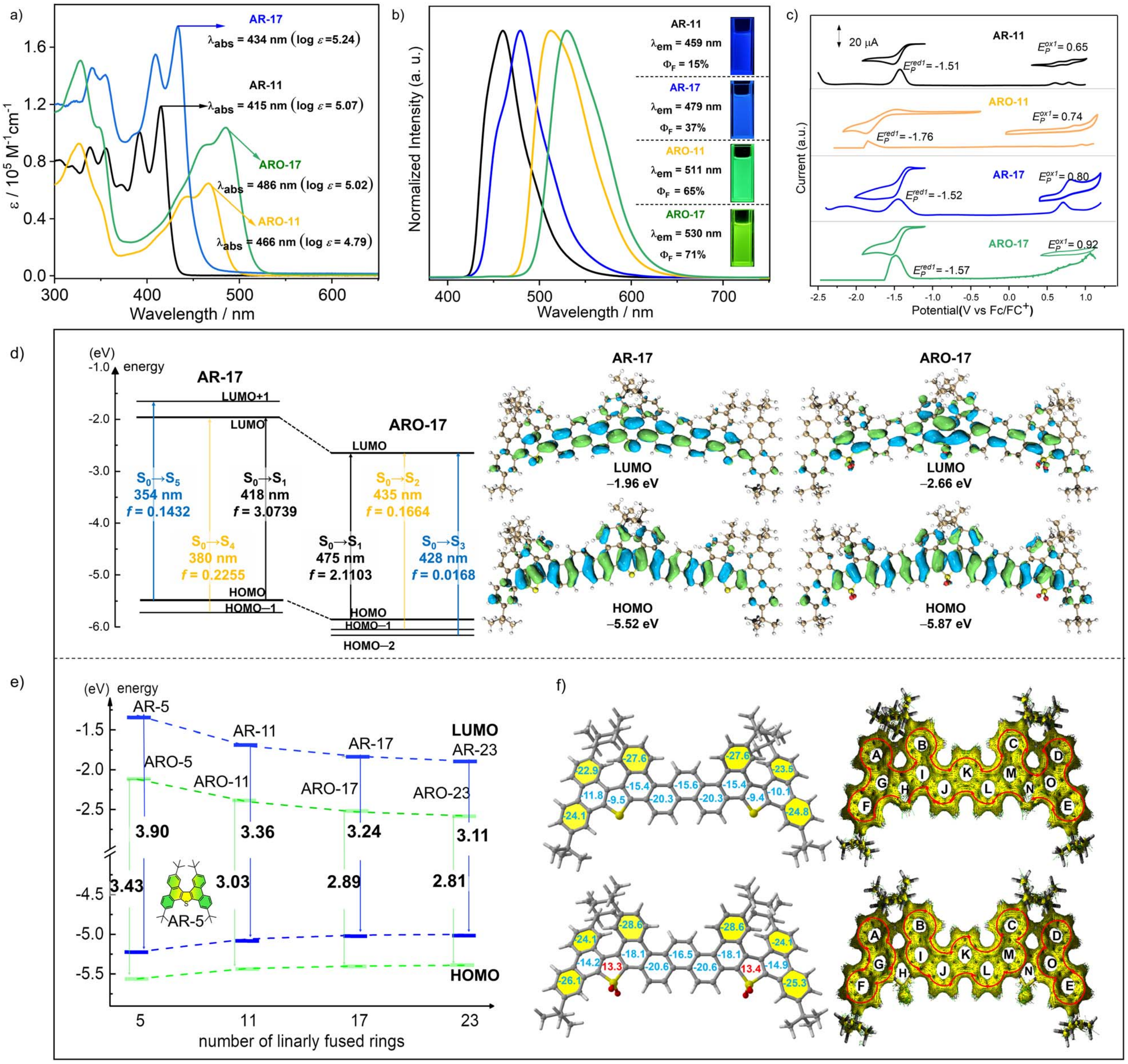

Fig. 4 Photophysical properties and TD-DFT calculations. (a) UV/vis absorption spectra (**AR-11**: black line; **AR-17**: blue line; **ARO-11**: orange line; **ARO-17**: green line) in CH_2Cl_2 solution. (b) photoluminescence spectrum in CH_2Cl_2 solution ($\lambda_{ex} = 300$ nm). (c) CV and DPV of **AR-11**, **ARO-11** and **AR-17**, **ARO-17** in CH_2Cl_2 solution containing 0.1 M Bu_4NPF_6 at room temperature at a scan rate of 0.1 V s^{-1}. (1.0×10^{-4} mol L^{-1} in CH_2Cl_2 for CV and DPV). (d) Energy diagrams and frontier molecular orbitals of **AR-17** and **ARO-17** calculated at the PBE0-D3(BJ)/6-31G(d,p) level of theory (unit: eV). (e) HOMO and LUMO energies of **AR-*n*** (blue dotted line) and **ARO-*n*** (green dotted line), calculated at the B3LYP/6-31G(d) level of theory. (f) Calculated NICS$(1)_{ZZ}$ values and ACID plots (contribution from π electrons only) of **AR-11** and **ARO-11** at the B3LYP/6-31G(d) level of theory. Aromatic sextet rings are shown in yellow.

observed from **AR-5** to **AR-23,** which leads to a clear shrinkage of E_g in the same sequence. The decreased HOMO level for **ARO-*n*** compared with **AR-*n*** strongly suggests the enhanced affinity of **ARO-*n*** to electrons.

Notably, to illustrate the electronic structures and the molecular aromaticity of *S*-doped GNRs, nucleus-independent chemical shift (NICS) and anisotropy of the induced current density (ACID) calculations on **AR-11** and **ARO-11** are conducted at the B3LYP/6-31G(d) level of theory based on the optimized structures (Fig. 4f, S17 and S18†).[52] The largely negative NICS$(1)_{ZZ}$ values (−22.9 to −27.6 of **AR-11** and −24.1 to −28.6 of **ARO-11** in yellow) indicate that these six-membered rings exhibit local aromaticity. These analyses are further supported by ACID calculations, which show clockwise (diamagnetic) ring currents mainly distributed at hexagonal rings A/B/C/D/E/F at the outer rims of the whole π-framework. In addition, rings J/L in **AR-11** and **ARO-11** also display very negative NICS$(1)_{ZZ}$ values (−20.3 of **AR-11** and −20.6 of **ARO-11**), manifesting that they also contribute to the aromatic structures. However, the positive NICS$(1)_{ZZ}$ values of 13.3 suggest that these sulfur dioxide rings have no contribution to the overall π-conjugation in Fig. 4f. The induced ring currents are relatively weak in the fused sulfur

Table 1 Spectroscopic characterization and energy levels of **AR-11**, **AR-17**, **ARO-11**, and **ARO-17**

Compound	λ_{abs} [a][nm]	ε_{max} [a][10^5 M^{-1} cm^{-1}]	λ_{em} [a][nm]	Φ [a,c][%]	τ [a,d][ns]	λ_{em} [b][nm]	Φ [b,c][%]	τ [b,d][ns]	E_{HOMO} [e][eV]	E_{HOMO} [f][eV]	E_{LUMO} [f][eV]	E_g [f][eV]
AR-11	415/392	1.19/1.01	459	15	2.07	464	4.7	0.67	−5.34	−5.06	−1.70	3.36
AR-17	434/410	1.74/1.56	479	37	4.02	506	0.2	0.54	−5.66	−5.03	−1.79	3.24
ARO-11	466/441	0.65/0.56	511	65	1.77	529	5.9	0.74	−5.60	−5.43	−2.40	3.03
ARO-17	486/463	1.04/0.92	530	71	1.77	549	1.5	1.24	−5.41	−5.40	−2.51	2.89

[a] Measured in CH_2Cl_2 solution (1.0×10^{-5} M). [b] Measured in the solid state. [c] Fluorescence quantum yield. [d] Fluorescence lifetime. [e] From CVs measured in DCM (1.0×10^{-4} M). The HOMO energy levels are adjusted according to the redox half potential of Fc/Fc^+ and estimated according to the formula E_{HOMO} (eV) = $-(4.80 + E_{onset}^{ox1} - E_{(Fc/Fc^+)})$ (also see Scheme S5). [f] Calculations were performed at the B3LYP/6-31G(d) level.

dioxide rings H/N of **ARO-11**, resulting in a break for the global delocalization of the π-electrons (Fig. 4f). These results demonstrate that the doping of sulfur dioxide achieves the delocalization of π-electrons in GNRs.

Conclusions

Graphene nanoribbons (GNRs) hold significant promise for optoelectronic applications, but their development is hampered by the limitations of traditional iterative synthetic methods. These methods often involve complex and expensive starting materials, restricting structural and functional diversity. This hinders the rapid exploration of structure–property relationships, especially length-dependent properties of GNRs, and the discovery of high-performance materials. A more efficient approach is to employ a modular synthesis, using end blocks, link blocks, and functional blocks as key components. This strategy allows for the facile synthesis of GNRs with a wide range of structures and functionalities by simply varying the functional block. We have demonstrated a highly efficient synthetic approach for sulfur-doped GNRs featuring a unique cove-armchair-fjord edge combination. Notably, sulfur incorporation into the backbone yielded arc-shaped GNRs. The unambiguous crystallographic characterization of **AR-11** and **ARO-11** reveals that the combined cove and fjord edge structure causes it to deviate from planarity due to steric repulsion. By oxidizing the electron-rich sulfur atoms to electron-deficient sulfones, we effectively tune the electronic properties of GNRs. Expanding the GNR family further, we're currently exploring the versatility of 1,8-diaryl phenanthrene by crafting GNRs with diverse functional blocks.

Data availability

The crystallographic data for **AR-11** and **ARO-11** reported in this article have been deposited at the Cambridge Crystallographic Data Centre (CCDC) under deposition numbers CCDC: 2303699 and 2303698, respectively. Other data supporting this study are available in the article and ESI.†

Author contributions

Y. L. conceived and directed the project. K. Y. directed the electrochemical synthesis section. R. Z. conducted most of the experiments. X. C. performed the DFT calculations. L. Z. and Y. H. and Z. Z. contributed to the synthesis. Q. W. and L. W. and T. W. analyzed the data. W. W. conducted the electrochemical synthesis. All authors discussed the results and commented on the manuscript.

Conflicts of interest

The authors declare no competing interests.

Acknowledgements

Project supported by the Joint Funds of the National Natural Science Foundation of China (No. U24A20567) and the Natural Science Foundation of Fujian Province, China (No. 2024J01236). We thank Prof. Weiguo Huang (Fujian Institute of Research on the Structure of Matter, Chinese Academy of Sciences) for the single crystal measurement and Prof. Kenichiro Itami (Nagoya University), Prof. Akiko Yagi (Nagoya University), Prof. Chenguang Wang (Jilin University) and Prof. Chaolumen (Inner Mongolia University) for constructive criticism of the manuscript.

Notes and references

1 J. Wu, W. Pisula and K. Müllen, Graphenes as Potential Material for Electronics, *Chem. Rev.*, 2007, **107**(3), 718–747.

2 X. Li, X. Wang, L. Zhang, S. Lee and H. Dai, Chemically Derived, Ultrasmooth Graphene Nanoribbon Semiconductors, *Science*, 2008, **319**(5867), 1229–1232.

3 Y. Segawa, H. Ito and K. Itami, Structurally uniform and atomically precise carbon nanostructures, *Nat. Rev. Mater.*, 2016, **1**(1), 15002.

4 K.-Y. Yoon and G. Dong, Liquid-phase bottom-up synthesis of graphene nanoribbons, *Mater. Chem. Front.*, 2020, **4**(1), 29–45.

5 Y. Yano, N. Mitoma, H. Ito and K. Itami, A Quest for Structurally Uniform Graphene Nanoribbons: Synthesis, Properties, and Applications, *J. Org. Chem.*, 2020, **85**(1), 4–33.

6 R. S. K. Houtsma, J. de la Rie and M. Stöhr, Atomically precise graphene nanoribbons: interplay of structural and electronic properties, *Chem. Soc. Rev.*, 2021, **50**(11), 6541–6568.

7 Y. Gu, Z. Qiu and K. Müllen, Nanographenes and Graphene Nanoribbons as Multitalents of Present and Future Materials Science, *J. Am. Chem. Soc.*, 2022, **144**(26), 11499–11524.

8 M.-W. Wang, W. Fan, X. Li, Y. Liu, Z. Li, W. Jiang, J. Wu and Z. Wang, Molecular Carbons: How Far Can We Go?, *ACS Nano*, 2023, **17**(21), 20734–20752.

9 O. V. Yazyev, A Guide to the Design of Electronic Properties of Graphene Nanoribbons, *Acc. Chem. Res.*, 2013, **46**(10), 2319–2328.

10 J. Liu, B.-W. Li, Y.-Z. Tan, A. Giannakopoulos, C. Sanchez-Sanchez, D. Beljonne, P. Ruffieux, R. Fasel, X. Feng and K. Müllen, Toward Cove-Edged Low Band Gap Graphene Nanoribbons, *J. Am. Chem. Soc.*, 2015, **137**(18), 6097–6103.

11 X. Yao, W. Zheng, S. Osella, Z. Qiu, S. Fu, D. Schollmeyer, B. Müller, D. Beljonne, M. Bonn, H. I. Wang, K. Müllen and A. Narita, Synthesis of Nonplanar Graphene Nanoribbon with Fjord Edges, *J. Am. Chem. Soc.*, 2021, **143**(15), 5654–5658.

12 Y. Wang, Y. Huang, T. Huang, J. Zhang, T. Luo, Y. Ni, B. Li, S. Xie and Z. Zeng, Perylene-Based Linear Nonalternant Nanoribbons with Bright Emission and Ambipolar Redox Behavior, *Angew. Chem., Int. Ed.*, 2022, **61**(21), e202200855.

13 K. Liu, W. Zheng, S. Osella, Z.-L. Qiu, S. Böckmann, W. Niu, L. Meingast, H. Komber, S. Obermann, R. Gillen, M. Bonn, M. R. Hansen, J. Maultzsch, H. I. Wang, J. Ma and X. Feng, Cove-Edged Chiral Graphene Nanoribbons with Chirality-Dependent Bandgap and Carrier Mobility, *J. Am. Chem. Soc.*, 2024, **146**(1), 1026–1034.

14 S. Kawai, S. Nakatsuka, T. Hatakeyama, R. Pawlak, T. Meier, J. Tracey, E. Meyer and A. S. Foster, Multiple heteroatom substitution to graphene nanoribbon, *Sci. Adv.*, 2018, **4**(4), eaar7181.

15 X.-Y. Wang, X. Yao, A. Narita and K. Müllen, Heteroatom-Doped Nanographenes with Structural Precision, *Acc. Chem. Res.*, 2019, **52**(9), 2491–2505.

16 A. Borissov, Y. K. Maurya, L. Moshniaha, W.-S. Wong, M. Żyła-Karwowska and M. Stępień, Recent Advances in Heterocyclic Nanographenes and Other Polycyclic Heteroaromatic Compounds, *Chem. Rev.*, 2022, **122**(1), 565–788.

17 Y. Sano, T. Shintani, M. Hayakawa, S. Oda, M. Kondo, T. Matsushita and T. Hatakeyama, One-Shot Construction of BN-Embedded Heptadecacene Framework Exhibiting Ultra-narrowband Green Thermally Activated Delayed Fluorescence, *J. Am. Chem. Soc.*, 2023, **145**(21), 11504–11511.

18 L. Chen, Y. Hernandez, X. Feng and K. Müllen, From Nanographene and Graphene Nanoribbons to Graphene Sheets: Chemical Synthesis, *Angew. Chem., Int. Ed.*, 2012, **51**(31), 7640–7654.

19 J. Liu and X. Feng, Synthetic Tailoring of Graphene Nanostructures with Zigzag-Edged Topologies: Progress and Perspectives, *Angew. Chem., Int. Ed.*, 2020, **59**(52), 23386–23401.

20 W. Chen, F. Yu, Q. Xu, G. Zhou and Q. Zhang, Recent Progress in High Linearly Fused Polycyclic Conjugated Hydrocarbons (PCHs, $n > 6$) with Well-Defined Structures, *Adv. Sci.*, 2020, **7**(12), 1903766.

21 A. Jolly, D. Miao, M. Daigle and J.-F. Morin, Emerging Bottom-Up Strategies for the Synthesis of Graphene Nanoribbons and Related Structures, *Angew. Chem., Int. Ed.*, 2020, **59**(12), 4624–4633.

22 M. Grzybowski, K. Skonieczny, H. Butenschön and D. T. Gryko, Comparison of Oxidative Aromatic Coupling and the Scholl Reaction, *Angew. Chem., Int. Ed.*, 2013, **52**(38), 9900–9930.

23 Y. Zhang, S. H. Pun and Q. Miao, The Scholl Reaction as a Powerful Tool for Synthesis of Curved Polycyclic Aromatics, *Chem. Rev.*, 2022, **122**(18), 14554–14593.

24 Y. Zhong, B. Kumar, S. Oh, M. T. Trinh, Y. Wu, K. Elbert, P. Li, X. Zhu, S. Xiao, F. Ng, M. L. Steigerwald and C. Nuckolls, Helical Ribbons for Molecular Electronics, *J. Am. Chem. Soc.*, 2014, **136**(22), 8122–8130.

25 M. Daigle, A. Picard-Lafond, E. Soligo and J.-F. Morin, Regioselective Synthesis of Nanographenes by Photochemical Cyclodehydrochlorination, *Angew. Chem., Int. Ed.*, 2016, **55**(6), 2042–2047.

26 K. Kato, Y. Segawa, L. T. Scott and K. Itami, A Quintuple [6] Helicene with a Corannulene Core as a C5-Symmetric Propeller-Shaped π-System, *Angew. Chem., Int. Ed.*, 2018, **57**(5), 1337–1341.

27 W. Hagui, H. Doucet and J.-F. Soulé, Application of Palladium-Catalyzed C(sp2)–H Bond Arylation to the Synthesis of Polycyclic (Hetero)Aromatics, *Chem*, 2019, **5**(8), 2006–2078.

28 W. Yang, A. Lucotti, M. Tommasini and W. A. Chalifoux, Bottom-Up Synthesis of Soluble and Narrow Graphene Nanoribbons Using Alkyne Benzannulations, *J. Am. Chem. Soc.*, 2016, **138**(29), 9137–9144.

29 Y. L. Li, C.-T. Zee, J. B. Lin, V. M. Basile, M. Muni, M. D. Flores, J. Munárriz, R. B. Kaner, A. N. Alexandrova, K. N. Houk, S. H. Tolbert and Y. Rubin, Fjord-Edge Graphene Nanoribbons with Site-Specific Nitrogen Substitution, *J. Am. Chem. Soc.*, 2020, **142**(42), 18093–18102.

30 A. Narita, Z. Chen, Q. Chen and K. Müllen, Solution and on-surface synthesis of structurally defined graphene nanoribbons as a new family of semiconductors, *Chem. Sci.*, 2019, **10**(4), 964–975.

31 X. Yang, S. M. Elbert, F. Rominger and M. Mastalerz, A Series of Soluble Thieno-Fused Coronene Nanoribbons of Precise Lengths, *J. Am. Chem. Soc.*, 2022, **144**(22), 9883–9892.

32 A. Boddeda, M. M. Hossain, M. Saeed Mirzaei, S. V. Lindeman, S. Mirzaei and R. Rathore, Angular ladder-type meta-phenylenes: synthesis and electronic structural analysis, *Org. Chem. Front.*, 2020, **7**(20), 3215–3222.

33 R. Jasti, J. Bhattacharjee, J. B. Neaton and C. R. Bertozzi, Synthesis, Characterization, and Theory of [9]-, [12]-, and [18]Cycloparaphenylene: Carbon Nanohoop Structures, *J. Am. Chem. Soc.*, 2008, **130**(52), 17646–17647.

34 Y. Segawa, S. Miyamoto, H. Omachi, S. Matsuura, P. Šenel, T. Sasamori, N. Tokitoh and K. Itami, Concise Synthesis and Crystal Structure of [12]Cycloparaphenylene, *Angew. Chem., Int. Ed.*, 2011, **50**(14), 3244–3248.

35 L. Zhu, J. Xu, B. Lan, X. Chen, H. Kono, H. Xu, J. Yan, W. Li, A. Yagi, Y. Yuan, K. Itami and Y. Li, Ferrocene-based conjugated macrocycles: shotgun synthesis, size-dependent

properties and tunable fluorescence intensity, *Org. Chem. Front.*, 2024, **11**(18), 5130–5137.

36 J. Xu, B. Lan, L. Zhu, H. Xu, X. Chen, W. Li, Y. Yuan, J. Yan and Y. Li, Synthesis and Properties of Ferrocene Conjugated Macrocycles with Illusory Topology of the Penrose Stairs, *Chem. Res. Chin. Univ.*, 2024, **40**(5), 881–886.

37 B. Lan, J. Xu, L. Zhu, X. Chen, H. Kono, P. Wang, X. Zuo, J. Yan, A. Yagi, Y. Zheng, S. Chen, Y. Yuan, K. Itami and Y. Li, Side-Chain Type Ferrocene Macrocycles, *Precis. Chem.*, 2024, **2**(4), 143–150.

38 Y. Li, A. Yagi and K. Itami, Synthesis of sterically hindered 4,5-diarylphenanthrenes *via* acid-catalyzed bisannulation of benzenediacetaldehydes with alkynes, *Chem. Sci.*, 2019, **10**(21), 5470–5475.

39 When 2-bromo-4,4'-di-*tert*-butyl-1,1'-biphenyl was employed as the end-capping compound, the yields of **4a** and **4b** decreased to 30% and 16%, respectively (Scheme S3†).

40 See the ESI† for a full citation of Gaussian 16.

41 F. Neese, Software update: The ORCA program system—Version 5.0, *WIREs Com. Mol. Sci.*, 2022, **12**(5), e1606.

42 F. Neese, Software update: the ORCA program system, version 4.0, *WIREs Com. Mol. Sci.*, 2018, **8**(1), e1327.

43 N. Mardirossian and M. Head-Gordon, ωB97M-V: A combinatorially optimized, range-separated hybrid, meta-GGA density functional with VV10 nonlocal correlation, *J. Chem. Phys.*, 2016, **144**, 214110.

44 J.-D. Chai and M. Head-Gordon, Long-range corrected hybrid density functionals with damped atom–atom dispersion corrections, *Phys. Chem. Chem. Phys.*, 2008, **10**(44), 6615–6620.

45 F. Weigend, Accurate Coulomb-fitting basis sets for H to Rn, *Phys. Chem. Chem. Phys.*, 2006, **8**(9), 1057–1065.

46 F. Weigend and R. Ahlrichs, Balanced basis sets of split valence, triple zeta valence and quadruple zeta valence quality for H to Rn: Design and assessment of accuracy, *Phys. Chem. Chem. Phys.*, 2005, **7**(18), 3297–3305.

47 C. Würth, M. Grabolle, J. Pauli, M. Spieles and U. Resch-Genger, Relative and absolute determination of fluorescence quantum yields of transparent samples, *Nat. Protoc.*, 2013, **8**(8), 1535–1550.

48 D. L. Dexter and J. H. Schulman, Theory of Concentration Quenching in Inorganic Phosphors, *J. Chem. Phys.*, 1954, **22**, 1063–1070.

49 M. Kasha, H. Rawls and M. El-Bayoumi, The exciton model in molecular spectroscopy, *Pure Appl. Chem.*, 1965, **11**, 371–392.

50 R. F. Chen and J. R. Knutson, Mechanism of fluorescence concentration quenching of carboxyfluorescein in liposomes: energy transfer to nonfluorescent dimers, *Anal. Biochem.*, 1988, **172**(1), 61–77.

51 T. Lu and F. Chen, Multiwfn: A multifunctional wavefunction analyzer, *J. Comput. Chem.*, 2012, **33**(5), 580–592.

52 M. Randić, Aromaticity of Polycyclic Conjugated Hydrocarbons, *Chem. Rev.*, 2003, **103**(9), 3449–3606.